RSC Advances

PAPER

View Article Online
View Journal | View Issue

Cite this: *RSC Adv.*, 2026, **16**, 10243

Construction of ZnS/CdS/Ti^{3+}-TiO_2 heterojunction: synergistic enhancement of visible light harvesting and photocathodic protection performance

Wenhao Liu,[ac] Yanfeng Zhu, *[ab] Zhihao Liu[ab] and Jianxia Gou[ab]

Marine corrosion poses a critical threat to the safety of offshore oil and gas facilities. To address the intrinsic drawbacks of pristine TiO_2, ZnS/CdS/Ti^{3+}-TiO_2 nanotube composites were rationally fabricated *via* a synergistic strategy combining electrochemical anodization and successive ionic layer adsorption and reaction (SILAR) techniques. Structural and optical characterization confirmed that the as-synthesized composites feature a well-constructed cascade band alignment, which efficiently mitigates the recombination of photogenerated electron–hole pairs. Accordingly, the optimized photoanode delivered a high photocurrent density of 279 μA cm^{-2}. When coupled with 316 stainless steel (316 SS), the composite exhibited a pronounced photo-induced potential of −0.89 V (*vs.* SCE), achieving a remarkable performance enhancement over pristine TiO_2. This enhanced photocathodic protection originates from the synergistic interplay between Ti^{3+} self-doping and the ZnS/CdS heterojunction: Ti^{3+} self-doping introduces abundant electron donors to enhance the electrical conductivity of the composite, whereas the ZnS/CdS heterojunction broadens the visible-light absorption range and accelerates the separation and directional migration of photogenerated charge carriers.

Received 26th November 2025
Accepted 14th February 2026

DOI: 10.1039/d5ra09129b

rsc.li/rsc-advances

1. Introduction

Metallic materials, due to their outstanding mechanical properties and workability, are extensively employed in the construction of offshore oil and gas transportation infrastructure. Nevertheless, the marine environment-characterized by intense sunlight, high humidity, and high salinity-renders these facilities particularly vulnerable to corrosion.[1–3] Such corrosion not only compromises structural integrity but can also result in environmental pollution, ecosystem disruption, risks to human safety, and substantial economic losses.[4] Therefore, the development of efficient, environmentally friendly, and sustainable corrosion protection technologies is crucial for ensuring the long-term safe operation of oil and gas transportation facilities.[5,6]

Photocathodic protection (PCP), as an emerging anticorrosion technology, utilizes photoanode materials to capture light energy and transfer photogenerated electrons to the metal substrate, thereby providing cathodic protection.[7,8] Due to its energy efficiency, environmental friendliness and potential for long-term protection, PCP has demonstrated considerable promise in marine corrosion prevention.[9] In recent years, with the rapid advancement of photoelectronic materials, semiconductors possessing excellent photoelectric conversion properties have been increasingly integrated into PCP systems, offering novel strategies to tackle metal corrosion challenges.[10]

One-dimensional TiO_2 nanotube arrays fabricated by anodic oxidation have been extensively investigated and applied in PCP because of their high chemical stability, non-toxicity, large specific surface area, and outstanding photoelectric properties.[11–13] However, TiO_2 still has inherent limitations: its wide bandgap (~3.2 eV) restricts light absorption mainly to the ultraviolet region, resulting in low solar energy utilization, the fast recombination of photogenerated electron–hole pairs reduces charge utilization efficiency, and its limited charge storage capacity makes it difficult to maintain protection for stainless steel under dark conditions.[14–16] These drawbacks significantly hinder its practical application in marine corrosion protection, highlighting the need for further modification of TiO_2.

Sulfide semiconductors, characterized by their narrow bandgaps (~2.5 eV) and excellent visible-light absorption properties, have attracted considerable attention in the field of photoelectronic devices.[17,18] When integrated with TiO_2 to construct heterojunctions, they can effectively expand the photoresponse range and facilitate charge carrier separation. Representative systems include PbS/TiO_2,[19,20] CdS/TiO_2 (ref. 21 and 22), Bi_2S_3/TiO_2 (ref. 23 and 24) and $CuInS_2$/TiO_2.[25,26] Actually, the strategy of constructing heterostructures to boost

[a]*College of Chemical Engineering and Materials, Shandong University of Aeronautics, Binzhou, Shandong 256600, PR China. E-mail: yanfengzhu2014@163.com*
[b]*Binzhou Key Laboratory of Applied Electrochemistry, Binzhou, Shandong 256600, PR China*
[c]*Shandong Key Laboratory of Eco-Environmental Science for the Yellow River Delta, Binzhou, Shandong 256600, PR China*

performance has been widely proven across various material systems. Recent studies have highlighted the enhanced optical properties of nanoplatelet-embedded ZnSe/Bi_2Se_3 core/shell quantum dots,[27] the improved optoelectronic and dielectric applications of SnS/MnSe heterostructures[28] and the critical role of interface engineering in $SnSe_2$/TiO_2 photodetectors.[29] Among these, CdS stands out in photoelectric conversion and photocatalysis due to its narrow bandgap and high electron injection efficiency; however, its poor stability under illumination significantly limits practical use. To overcome this, coating CdS with a wide-bandgap semiconductor has been widely adopted to enhance its stability. ZnS, a non-toxic and chemically stable wide-bandgap (~3.8 eV) semiconductor, can form a protective shell on CdS, effectively suppressing photocorrosion and improving the visible-light stability of composite photoanodes.[30] Additionally, Ti^{3+} self-doping introduces oxygen vacancies into TiO_2, which can significantly enhance its electrical conductivity and visible-light absorption.[31,32]

Considering the above aspects, in this work, TiO_2 nanotubes were employed as the substrate, Ti^{3+} self-doping was introduced *via* electrochemical reduction, followed by the deposition of CdS and ZnS on the surface through successive ionic layer adsorption and reaction (SILAR) to fabricate ZnS/CdS/Ti^{3+} self-doped TiO_2 composite photoanodes. The morphology and elemental valence states of the materials were characterized by SEM and XPS. Meanwhile, their photocathodic protection performance for 316 stainless steel under simulated solar illumination was systematically investigated using photoelectrochemical measurements. This study is intended to provide novel insights and technical guidance for the modification of TiO_2-based photoanodes and their application in marine corrosion protection.

2. Experimental section

2.1 Reagents and materials

Titanium foil (Ti, 99.99% purity) and 316 stainless steel (316 SS) were purchased from Beijing Gaodewei Metal Co., Ltd ammonium fluoride (NH_4F, AR), sodium chloride (NaCl, AR), anhydrous ethanol (AR), methanol (AR), sodium hydroxide (NaOH, AR), cadmium nitrate tetrahydrate ($Cd(NO_3)_2 \cdot 4H_2O$, AR), sodium sulfide nonahydrate ($Na_2S \cdot 9H_2O$, AR), acetone (AR), glycerol (AR), ammonium sulfate ($(NH_4)_2SO_4$, AR), zinc chloride ($ZnCl_2$, AR) were purchased from Aladdin (Shanghai, China).

2.2 Fabrication of ZnS/CdS/Ti^{3+}-TiO_2 nanotube composite film

TiO_2 nanotube arrays (TNAs) were prepared on the Ti foil by anodic oxidation. Titanium foil (10 mm × 10 mm × 1 mm; purity > 99%) was sequentially ultrasonically cleaned in acetone, anhydrous ethanol, and deionized water for 15 min each, followed by drying with nitrogen gas. The fabrication process of ZnS/CdS/Ti^{3+}-TiO_2 is illustrated in Fig. 1. The anodic oxidation was performed in a two-electrode system, with a Ti foil as the anode and a platinum sheet as the cathode. The electrolyte consisted of 60 vol% glycerol solution, 40 vol% H_2O, and 0.5 wt% NH_4F. The reaction was performed at 20 V for 1 h.

Ti^{3+} self-doped TiO_2 nanotube films were fabricated *via* electrochemical reduction. A three-electrode system was employed in the experiment, where TNAs served as the cathode, a platinum sheet as the anode, and a saturated calomel electrode (SCE) as the reference electrode. The electrochemical reduction process was performed in 1 M $(NH_4)_2SO_4$ electrolyte, with a constant current density of 2 mA cm^{-2}. Subsequently, the reduced samples were calcined in a tubular furnace under a nitrogen-protective atmosphere, heated from room temperature to 450 °C at a rate of 5 °C min^{-1}, and maintained at 450 °C for 2 h. The resulting samples were denoted as B-TiO_2.

CdS and ZnS were deposited onto B-TiO_2 *via* the successive ionic layer adsorption and reaction SILAR method to fabricate ZnS/CdS/B-TiO_2 composite photoanodes. The deposition process was as follows: B-TiO_2 was first immersed in 0.4 M $Cd(NO_3)_2$ aqueous solution for 60 s, after which it was rinsed with deionized water and dried under a nitrogen stream. Subsequently, the treated B-TiO_2 was immersed in 0.1 M Na_2S aqueous solution for 60 s, followed by repeated rinsing and drying steps. This sequence of immersion, rinsing and drying operations constitutes one complete SILAR cycle. The cycle was repeated 10, 15, and 20 times, with the resulting samples designated as CdS/B-TiO_2-*X*, where *X* corresponds to the number of cycles.

Finally, a ZnS thin layer was deposited onto the CdS/B-TiO_2 samples *via* SILAR technique. 0.6 M $ZnCl_2$ ethanol solution and

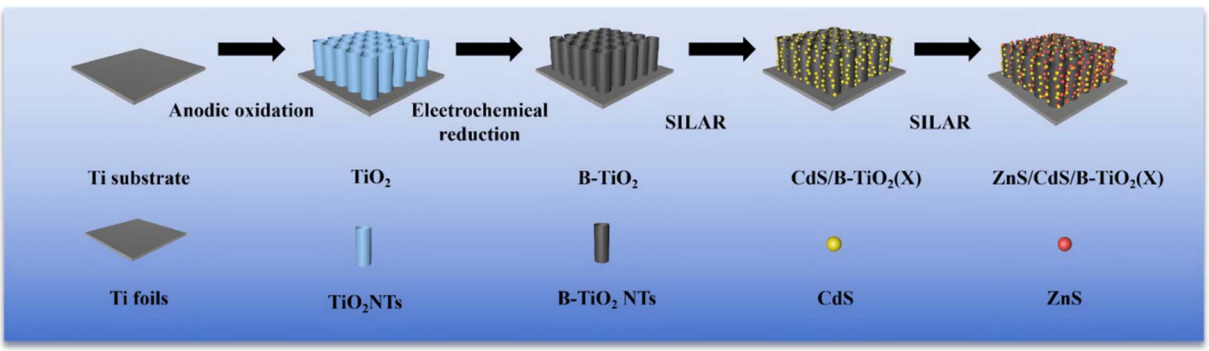

Fig. 1 Preparation of ZnS/CdS/B-TiO_2 nanotube composite films.

0.1 M Na_2S methanol solution were used as the Zn and S precursors. After 5 immersion cycles, the ZnS/CdS/B-TiO_2 sample was successfully obtained.

2.3 Characterisation

The surface morphology and elemental distribution were analyzed by scanning electron microscopy (SEM, Thermo Scientific) equipped with energy-dispersive X-ray spectroscopy (EDS), with an accelerating voltage of 20 kV. The crystal structure and phase composition of the samples were examined by X-ray diffraction (XRD, SmartLab SE) using Cu Kα radiation (λ = 1.5406 Å), from 10 to 80° with a scanning rate of $5°\cdot min^{-1}$. The elemental composition and chemical valence states were characterized by X-ray photoelectron spectroscopy (XPS, Thermo Scientific ESCALAB 250XI) using a monochromatic Al Kα (1486.6 eV) radiation source. All binding energies were calibrated with reference to the C 1s peak at 284.8 eV. The optical absorption properties of the samples were investigated by ultraviolet-visible (UV-Vis) spectroscopy (Hitachi U4100) in the wavelength range of 200–800 nm. In addition, photoluminescence (PL) spectra were recorded using a fluorescence lifetime and steady state spectrophotometer (FLS-980) with an excitation wavelength of 365 nm to evaluate the recombination behavior of photogenerated charge carriers.

2.4 Photoelectrochemical measurements

The photoelectrochemical properties were evaluated employing a Princeton Applied Research 2273 electrochemical workstation with a conventional three-electrode configuration. As shown in Fig. 2a, the as-prepared photoanodes were utilized as the working electrode, a saturated calomel electrode served as the reference electrode, and a platinum wire was applied as the counter electrode. A 500 W xenon lamp was used as the light source, and the light intensity at the photoanode surface was calibrated to 100 mW cm^{-2} using a radiometer. Photoelectrochemical measurements were conducted in an aqueous mixed solution containing 0.2 M NaOH and 0.1 M Na_2S. Mott–Schottky (MS) measurements were performed in a 0.1 M Na_2SO_4 aqueous solution at a constant frequency of 1000 Hz with an AC perturbation amplitude of 10 mV, over a potential range from −0.5 to 0.5 V.

2.5 Photocathodic protection measurements

To investigate the photocathodic protection properties, the open-circuit potential (OCP) variations and electrochemical impedance spectroscopy (EIS) of the 316 stainless steel (316 SS) electrode coupled with the photoanode were subsequently measured. The experimental setup consisted of a photoelectrolysis cell containing 0.2 M NaOH and 0.1 M Na_2S and a corrosion cell containing 3.5 wt% NaCl, which were interconnected *via* a salt bridge, as schematically illustrated in Fig. 2b. The 316 SS electrode was immersed in the corrosion cell, a saturated calomel electrode was used as the reference electrode, and a platinum sheet was used as the counter electrode. Under light irradiation conditions identical to those employed in the photoelectrochemical measurements, the potential variations were recorded continuously. The EIS measurements were performed in a frequency range from 10^5 to 10^{-2} Hz with an applied AC sinusoidal perturbation of 10 mV amplitude.[33,34]

3. Result and discussion

3.1 Characterization of films

Fig. 3 presents the SEM morphologies of TiO_2, B-TiO_2, and ZnS/CdS/B-TiO_2 samples. The B-TiO_2 nanotube arrays maintain a highly ordered, and intact structure, with distinct tube openings clearly observable. As the number of ZnS/CdS deposition cycles increases, the nanotube surfaces are gradually covered by nanoparticles, resulting in partial narrowing or even occlusion of the tube openings. For ZnS/CdS/B-TiO_2(10c), ZnS/CdS nanoparticles are uniformly distributed along the tube walls and openings; however, the surface coverage is relatively limited, leaving parts of the nanotubes exposed. This insufficient coverage may constrain light absorption and interfacial reaction activity. In contrast, ZnS/CdS/B-TiO_2(15c) exhibits more homogeneous and dense nanoparticle coverage, forming a continuous and stable composite configuration. Notably, the nanotube channels remain unobstructed without complete blockage, which facilitates the separation and transfer of photogenerated electrons. This morphology is deemed optimal. Nevertheless, for ZnS/CdS/B-TiO_2(20c), excessive deposition and aggregation of nanoparticles lead to substantial surface accumulation, with most tube openings blocked. This not only

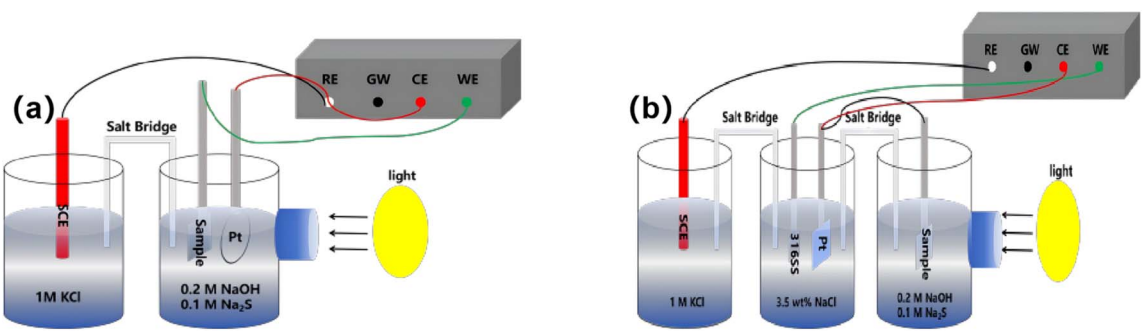

Fig. 2 Schematic illustration of the experimental setup for (a) photoelectrochemical and (b) photocathodic protection measurements.

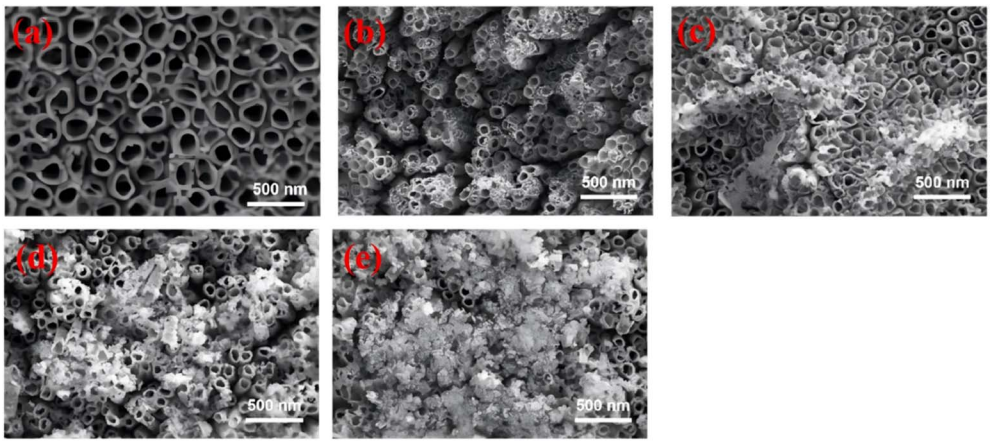

Fig. 3 SEM images of the different TiO_2 films: (a) TiO_2, (b) B-TiO_2, (c) ZnS/CdS/B-TiO_2(10c), (d) ZnS/CdS/B-TiO_2(15c) and (e) ZnS/CdS/B-TiO_2(20c).

reduces the specific surface area but also hinders electrolyte infiltration, potentially impairing charge transfer processes and photoelectrochemical conversion performance.

The elemental distribution and chemical composition of the ZnS/CdS/B-TiO_2(15c) sample was further investigated *via* EDS mapping and spectroscopy. As depicted in Fig. 4 of the corresponding results, Ti and O elements exhibited uniform distribution, which indicates that the structural integrity of the TiO_2 nanotube matrix was preserved. Meanwhile, Zn, Cd, and S elements were homogeneously dispersed across the surface-this confirms the successful deposition of ZnS and CdS onto TiO_2 nanotubes *via* SILAR method. Furthermore, the corresponding EDS spectrum in Fig. 4 displays distinct characteristic peaks corresponding to Ti, O, Zn, Cd, and S. The strong intensities of these signals verify the coexistence of ZnS and CdS phases within the composite, while the absence of other significant impurity peaks attests to the high chemical purity of the synthesized material. Notably, no significant aggregation of Zn, Cd, or S was observed, suggesting that with 15 deposition cycles, the composite nanoparticles achieved uniform surface coverage without excessive stacking or pore blockage. This result is consistent with the SEM observations, confirming that ZnS/CdS/B-TiO_2(15c) attains an optimal balance between morphology and composition. Such a favorable structure provides a solid structural basis for its superior photoelectrochemical activity and efficient photocathodic protection of 316 SS.

Fig. 5 presents the XRD patterns of pristine TiO_2, B-TiO_2, and ZnS/CdS/B-TiO_2 composite photoelectrodes with varying SILAR deposition cycles. As illustrated, all samples exhibit prominent diffraction peaks at 2θ = 25.3°, 37.8°, 48.0°, 53.9° and 55.1°, which are indexed to the (101), (004), (200), (105), and (211) planes of anatase TiO_2 (JCPDS no. 21-1272), respectively. Furthermore, the intense diffraction peaks observed at 35.1°, 38.4°, and 40.2° are attributed to the metallic Ti substrate, confirming that the TiO_2 nanostructures were grown directly onto the titanium surface. Comparing the patterns of pristine TiO_2 and B-TiO_2, it is evident that the characteristic peaks of the anatase phase show no significant shift after the self-doping treatment. This indicates that the introduction of Ti^{3+} ions

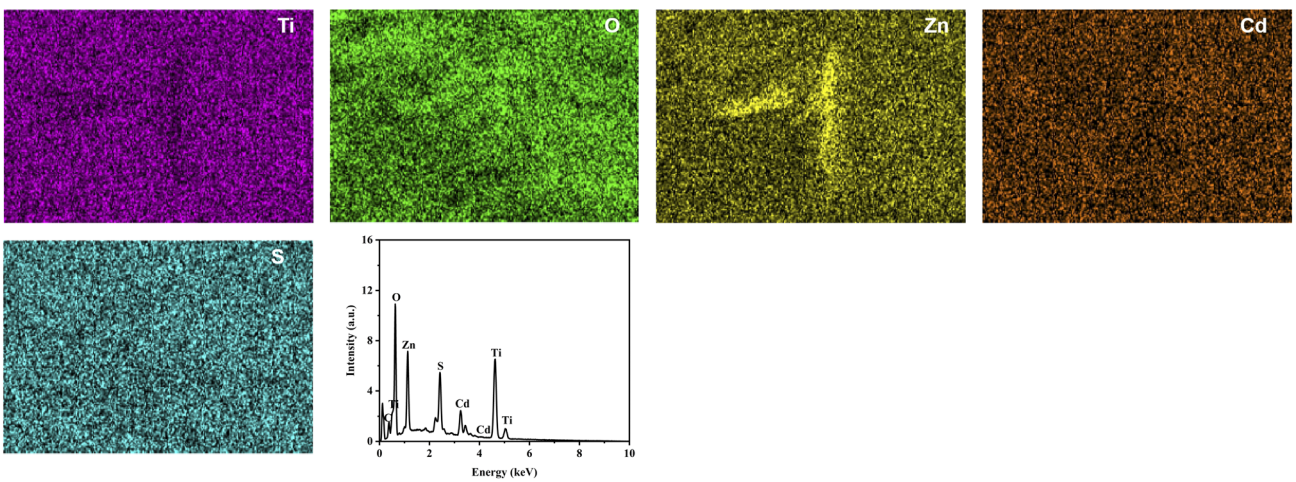

Fig. 4 EDS elemental mapping images of Ti, O, Zn, Cd, and S, and the corresponding EDS spectrum of the ZnS/CdS/B-TiO_2(15c) composite.

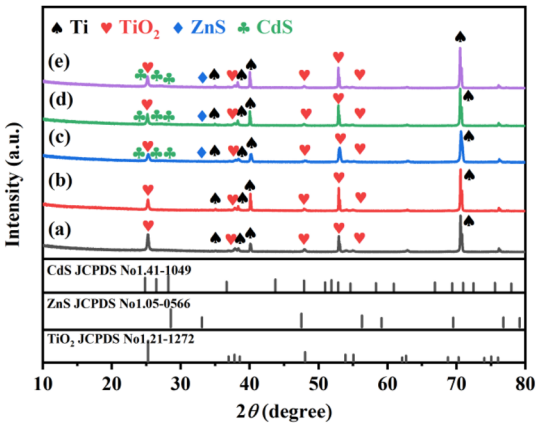

Fig. 5 XRD patterns of the different TiO_2 films: (a) TiO_2, (b) B-TiO_2, (c) ZnS/CdS/B-TiO_2(10c), (d) ZnS/CdS/B-TiO_2(15c) and (e) ZnS/CdS/B-TiO_2(20c).

and oxygen vacancies did not disrupt the long-range crystalline structure of TiO_2, maintaining its high crystallinity. For the ZnS/CdS/B-TiO_2 composite samples modified *via* the SILAR method, the primary signals in the original patterns correspond to the substrate and TiO_2. However, careful observation of the patterns reveals weak, broadened envelopes near $2\theta = 26.5°$ and 28.2° as the SILAR cycles increase from 10 to 20. These signals align with the (002) and (101) planes of hexagonal CdS (JCPDS no. 41-1049), respectively. The characteristic peaks of ZnS (*e.g.*, the (111) plane at 28.6°, JCPDS no. 05-0566) do not appear as distinct independent peaks due to significant overlapping with the TiO_2 and CdS signals, as well as the ultra-fine grain size. Such weak diffraction intensity is typically attributed to the low mass loading and the highly dispersed nanocrystalline nature of the chalcogenide sensitizers. The successful construction of these components will be further substantiated by the subsequent XPS elemental valence state analysis.

To verify the chemical composition and elemental valence states of the surface, X-ray photoelectron spectroscopy (XPS) analysis was performed, with the results shown in Fig. 6. Fig. 6 a presents the survey spectrum of the composite photoanode, featuring characteristic peaks corresponding to Ti, O, Cd, Zn, and S elements. This observation is consistent with the elemental composition inferred from EDS analysis, further confirming the successful construction of the composite system. As illustrated in Fig. 6b, the peaks at 458.95 eV and 464.67 eV are assigned to the Ti^{4+} $2p_{3/2}$ and Ti^{4+} $2p_{1/2}$ orbitals, respectively, while the weaker signals at 458.37 eV and 464.13 eV correspond to Ti^{3+} species, indicating partial reduction of Ti^{4+} in the TiO_2 matrix.[35] In Fig. 6c, the two deconvoluted peaks at 530.02 eV and 531.85 eV correspond to lattice oxygen (O^{2-}) in the TiO_2 crystal structure and surface-adsorbed oxygen (*e.g.*, H_2O), respectively.[36] Fig. 6d shows the high-resolution Cd 3d spectrum, where the peaks at 405.08 eV and 412.6 eV correspond to Cd $3d_{5/2}$ and Cd $3d_{3/2}$, respectively, consistent with the valence state of Cd^{2+} in CdS.[37] For the Zn 2p spectrum (Fig. 6e), the peaks located at 1022.0 eV and 1045.2 eV are attributed to Zn $2p_{3/2}$ and Zn $2p_{1/2}$, respectively, corresponding to Zn^{2+} in ZnS.[38] As shown in Fig. 6f, the S 2p spectrum exhibits two distinct peaks at 161.60 eV and 162.76 eV, which are assigned to S $2p_{3/2}$ and S $2p_{1/2}$, respectively-consistent with the S^{2-} valence state in ZnS and CdS.[39] Collectively, these XPS results confirm the successful synthesis of ZnS/CdS/B-TiO_2 composite photoanodes

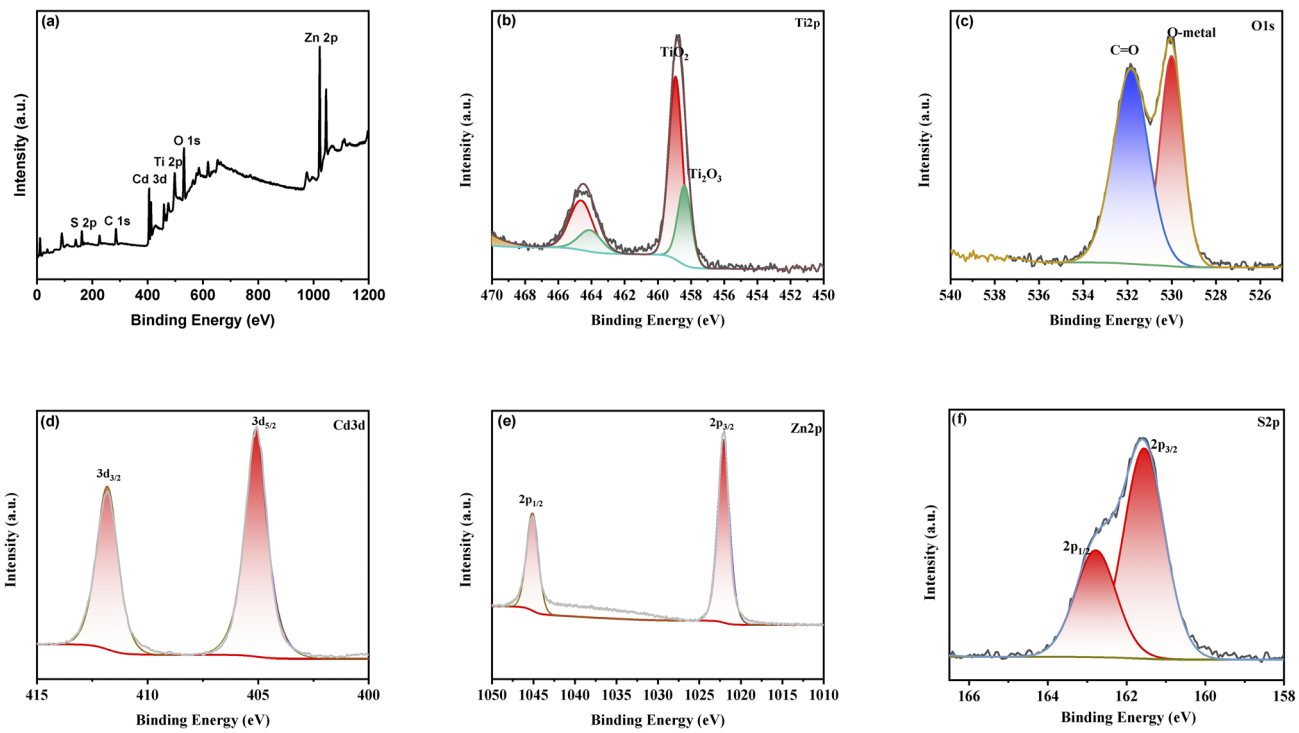

Fig. 6 XPS of ZnS/CdS/B-TiO_2 nanocomposite film, (a) survey spectra, (b) Ti 2p, (c) O 1s, (d) Cd 3d, (e) Zn 2p, (f) S 2p.

on the TiO_2 nanotubes surface, with all constituent elements existing in their expected chemical valence states.

The light-response properties of the TiO_2 nanocomposites within the wavelength range of 200–700 nm range were investigated using UV-vis diffuse reflectance spectroscopy (DRS), as shown in Fig. 7. As illustrated in Fig. 7a, the pristine TiO_2 nanotubes exhibit a characteristic absorption peak predominantly in the ultraviolet region, with an absorption edge centered around 380 nm. Following modification, the B-TiO_2, ZnS/CdS/B-TiO_2(10c), ZnS/CdS/B-TiO_2(15c), and ZnS/CdS/B-TiO_2(20c) samples all demonstrate a red-shift of the absorption edges and enhanced visible-light absorption. Notably, ZnS/CdS/B-TiO_2(15c) composite exhibits the strongest absorption intensity in the visible region. This enhancement is not due to a change in the intrinsic bandgap of the composite, but rather due to the efficient photon harvesting by the CdS/ZnS sensitizers and the intraband states induced by Ti^{3+} self-doping.[40]

The optical bandgap energies (E_g) of the semiconductors were estimated using the Tauc equation:[41–44]: $(\alpha h\nu)^{1/n} = A(h\nu - E_g)$, where $n = 2$ for the indirect transition of TiO_2.[11] The corresponding Tauc plots are presented in Fig. 7b. The calculated intrinsic bandgap for pristine TiO_2 is (3.16 ± 0.01) eV. For the self-doped B-TiO_2, the bandgap shifts to (2.89 ± 0.01) eV due to the introduction of mid-gap states. For the ZnS/CdS/B-TiO_2 composites, defining a single intrinsic bandgap is physically invalid due to their heterojunction nature. However, the Tauc analysis reveals that the apparent optical absorption onset shifts significantly to lower energies. Specifically, the ZnS/CdS/B-TiO_2(10c), ZnS/CdS/B-TiO_2(15c), and ZnS/CdS/B-TiO_2(20c) samples exhibit apparent absorption energies of (2.40 ± 0.01), (1.98 ± 0.01), and (2.03 ± 0.01) eV, respectively. Notably, the ZnS/CdS/B-TiO_2(15c) composite exhibits the lowest apparent energy barrier for photon excitation $(1.98 \pm 0.01$ eV). This implies a significantly broadened light-response range, laying a solid foundation for enhanced photoelectrochemical performance.

To investigate the separation and recombination dynamics of photogenerated electron–hole pairs, photoluminescence (PL) spectra were recorded, as shown in Fig. 8. Generally, PL

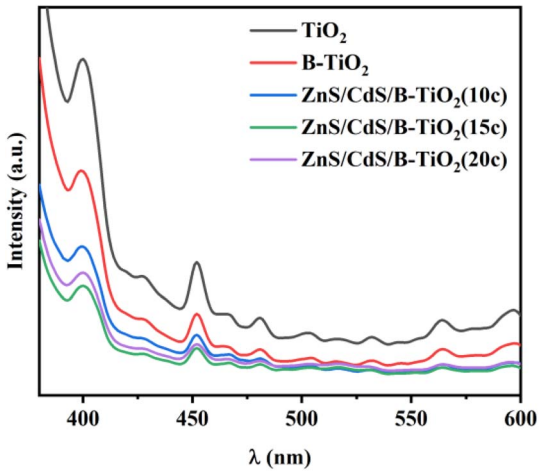

Fig. 8 PL spectra of different nanotube films.

emission originates from the radiative recombination of electrons and holes; accordingly, a lower PL intensity indicates more effective suppression of carrier recombination and higher charge separation efficiency. As observed, the pristine TiO_2 exhibits the highest emission intensity, with two distinct peaks centered at approximately 400 nm and 450 nm. This phenomenon is typically attributed to the radiative recombination of excitons at intrinsic surface states.[45] In the case of B-TiO_2, the PL intensity shows a noticeable decrease compared to pristine TiO_2. This quenching effect can be ascribed to the introduction of Ti^{3+} species and oxygen vacancies. These self-doped defects act as shallow electron traps and increase the donor density, which improves the electrical conductivity of the photoanode and facilitates the transport of photogenerated electrons, thereby reducing the probability of radiative recombination. Furthermore, upon the deposition of ZnS and CdS, the PL intensities of the ZnS/CdS/B-TiO_2 composites are significantly quenched. This drastic reduction confirms the successful construction of a heterojunction, where the built-in electric field drives the rapid transfer of carriers, effectively blocking the

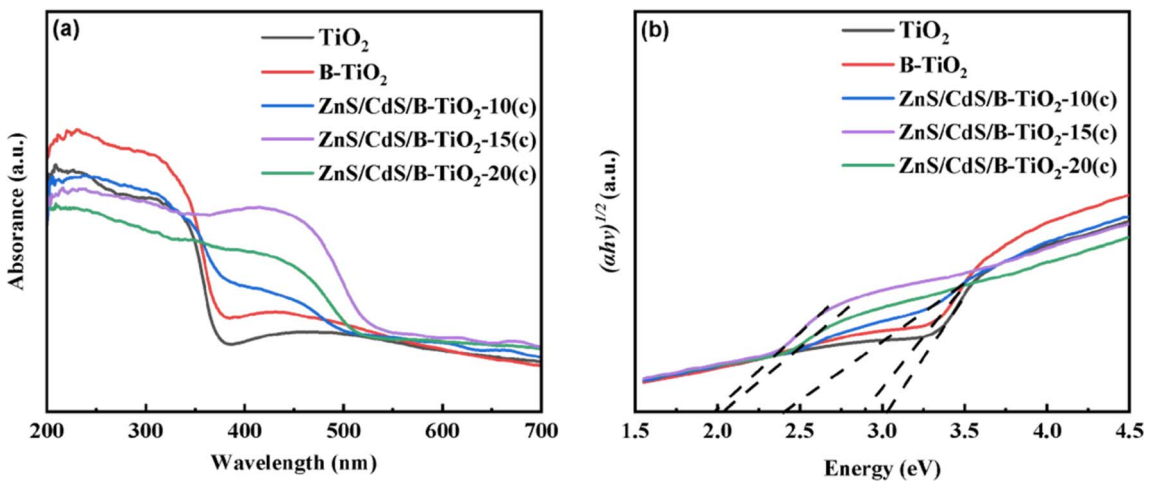

Fig. 7 (a) UV-vis diffuse reflection spectra of TiO_2 nanotube and TiO_2 nanocomposites and (b) Tauc plots of corresponding samples.

recombination pathway. Among the composites, the ZnS/CdS/B-TiO_2(15c) sample displays the lowest fluorescence intensity. This confirms that 15 SILAR cycles achieve the optimal balance between sensitizer loading and charge transfer resistance. The minimized PL intensity demonstrates that the synergistic effect of Ti^{3+} self-doping and heterojunction engineering maximizes the charge separation efficiency, which is consistent with the superior photo-electrochemical performance observed in the aforementioned tests.

3.2 Photoelectrochemical properties

To further evaluate the photoresponse behavior of TiO_2 and its composites, open-circuit potential (OCP) measurements were performed. Fig. 9 displays the potential–time curves of ZnS/CdS/B-TiO_2 films fabricated with different numbers of SILAR deposition cycles under intermittent xenon lamp illumination. Upon irradiation, the photon energy exceeds the bandgap of the material, triggering the separation of photogenerated electron–hole pairs. The substantial accumulation of photogenerated electrons at the sample surface induces a significant change in surface potential, which is manifested as a potential shift in the OCP curves. During the illumination period, the sample potential initially decreases rapidly and subsequently stabilizes at a steady-state value; when the light source is turned off, the potential gradually reverts to its dark-state level. This reversible potential variation reflects the kinetic delay of electron–hole recombination, a key feature of efficient photoelectrochemical systems. In the dark, the OCP values of TiO_2, B-TiO_2, ZnS/CdS/B-TiO_2(10c), ZnS/CdS/B-TiO_2(15c), and ZnS/CdS/B-TiO_2(20c) are −299 mV, −342 mV, −356 mV, −350 mV, and −314 mV, respectively. Under illumination, the potential drops by 61 mV, 133 mV, 371 mV, 526 mV, and 468 mV, respectively. Notably, ZnS/CdS/B-TiO_2(15c) composite exhibits the most significant potential drop upon illumination. These results indicate that the sample accumulates a greater number of photogenerated electrons and possesses a more efficient photoelectron transfer capability, thereby demonstrating superior photocathodic protection performance. Furthermore, multiple on/off cycles of illumination result in no significant potential fluctuation, demonstrating the excellent periodicity and reproducibility of the sample's photoresponse behavior, which is crucial for practical application in long-term corrosion protection.

To investigate intrinsic electrochemical properties of the photoanodes, such as charge-transfer resistance and carrier transport efficiency, electrochemical impedance spectroscopy (EIS) measurements were conducted on TiO_2 composite films prepared under different conditions, and simulated Nyquist plots were obtained as shown in Fig. 10. At the same frequency, a larger semicircle radius indicates a smaller capacitance, higher polarization resistance, greater energy barrier for electrode reactions, and consequently, slower reaction kinetics.[46]

As shown in Fig. 10, under illumination, the semicircle radii of different film electrodes follow the order: TiO_2 > B-TiO_2 > ZnS/CdS/B-TiO_2(10c) > ZnS/CdS/B-TiO_2(20c) > ZnS/CdS/B-TiO_2(15c). Evidently, the ZnS/CdS/B-TiO_2(15c) sample exhibits a relatively smaller semicircle radius, indicating superior photoelectric conversion performance. This suggests that ZnS/CdS/B-TiO_2(15c) is likely to demonstrate enhanced performance in photocathodic protection applications.

Photocurrent density is a key parameter for evaluating the photoelectric conversion performance of photoanodes; higher values indicate more efficient generation and separation of photogenerated charge carriers, as well as stronger photoelectric conversion capability.[47] Fig. 11 presents the photocurrent density–time (I–t) curves of TiO_2 photoanodes and their modified composites under intermittent illumination. At the moment of light activation, the modified TiO_2 photoanodes exhibit significantly higher instantaneous photocurrents, indicating an enhanced photoresponse capability. Under steady state, the photocurrent density of the pristine TiO_2 photoanode is approximately 20 μA cm^{-2}, while that of the B-TiO_2 photoanode reaches ~28 μA cm^{-2}. For the ZnS/CdS/B-TiO_2 composites, the photocurrent densities of ZnS/CdS/B-TiO_2(10c), ZnS/CdS/B-TiO_2(15c), and ZnS/CdS/B-TiO_2(20c) reach 195 μA cm^{-2}, 279 μA cm^{-2}, and 214 μA cm^{-2}, respectively, corresponding to 9.75, 13.95, and 10.7 times that of pristine TiO_2, respectively. The significant enhancement in photocurrent is primarily

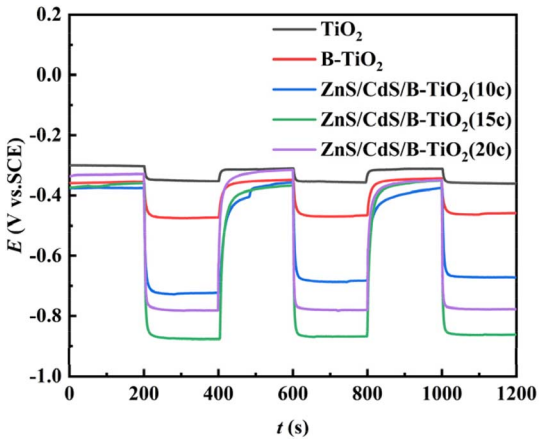

Fig. 9 OCP curves of TiO_2 and composite films under intermittent illumination.

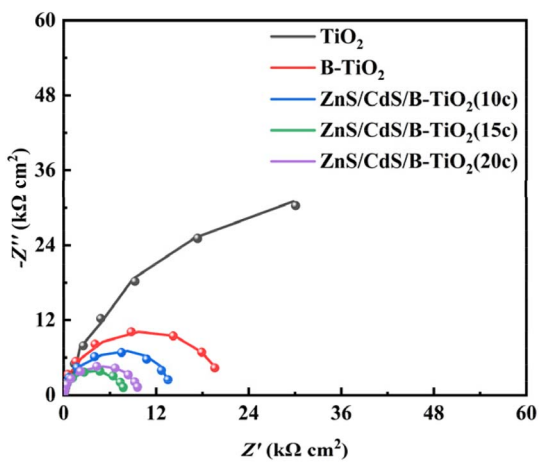

Fig. 10 Nyquist plots of TiO_2 and composite photoanodes.

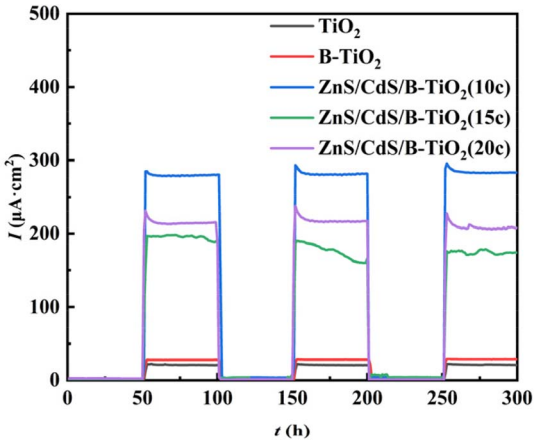

Fig. 11 The photoresponse spectra of pure TiO_2 NTs, B-TiO_2, and ZnS/CdS/B-TiO_2 NTs.

attributed to the synergistic modification by ZnS and CdS. This modification not only extends the absorption range of TiO_2 into the visible region but also effectively suppresses the recombination of photogenerated electron–hole pairs, thereby facilitating efficient carrier separation and transport and markedly improving the photoelectrical performance of the material.

3.3 Photocathodic protection properties

To evaluate the photocathodic protection performance of TiO_2 photoanodes and their composites for 316 SS under simulated seawater conditions, the potential variation of 316 SS coupled with TiO_2 or ZnS/CdS/B-TiO_2(15c) photoanodes was recorded under intermittent simulated solar illumination, as illustrated in Fig. 12. Upon illumination, photogenerated electrons transfer from the semiconductor material to the surface of 316 SS, resulting in a rapid reduction in potential. When the light is turned off, the potential gradually rebounds yet remains lower than the corrosion potential of 316 SS. The self-corrosion potential of 316 SS is approximately 0 V; when coupled with

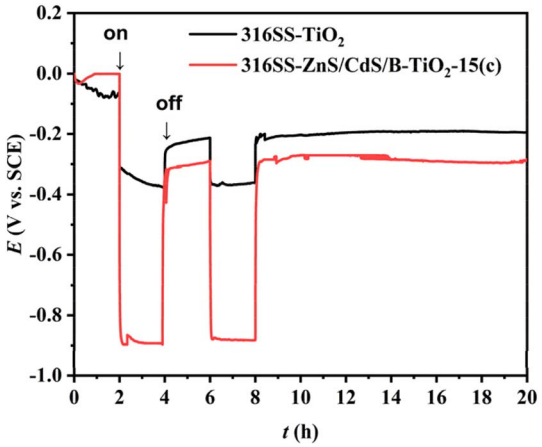

Fig. 12 The OCP curves of 316SS coupled to the different films under intermittent white light illumination.

pristine TiO_2, the potential decreases to around −0.37 V. In contrast, with the ZnS/CdS/B-TiO_2(15c) composite as the photoanode, the coupled potential drops to roughly −0.89 V, corresponding to a negative shift of ~890 mV. After two cycles of intermittent light illumination, the potential remains stable. Moreover, even after 15 h of immersion, the potential of 316 SS coupled with ZnS/CdS/B-TiO_2(15c) only exhibits slight fluctuations, indicating relatively stable potential over extended durations. These results demonstrate that the modification with ZnS and CdS enables prolonged and effective photocathodic protection for 316 SS.

To contextualize this performance, Table 1 presents a comparison with other recently reported TiO_2-based photoanodes. Notably, the ZnS/CdS/B-TiO_2(15c) composite exhibits a significantly more negative photo-potential (−0.89 V) than the counterparts listed. Furthermore, in terms of stability, it outperforms many reported electrodes, confirming its competitive advantage for practical marine applications.

To gain deeper insight into the interfacial charge-transfer behaviors of photoanodes in electrolyte solutions, and to further clarify their photocathodic protection mechanisms, electrochemical impedance spectroscopy (EIS) measurements were performed under simulated solar illumination. Fig. 13 presents the Nyquist plots of the 316 SS. In this equivalent circuit, R_s stands for the solution resistance; Q_f and R_f denote the capacitance and resistance of the surface film, respectively; and Q_{dl} and R_{ct} correspond to the double-layer capacitance and charge-transfer resistance. The bare 316 SS exhibits the largest semicircle radius in its Nyquist plot, which indicates a high charge-transfer resistance (R_{ct}) and restricted interfacial electron transport. After modification with a TiO_2 coating, the semicircle radius is significantly reduced, suggesting a decrease in charge-transfer resistance and an improvement in electron transport efficiency. Upon further incorporating ZnS/CdS into the partially reduced TiO_2, the ZnS/CdS/B-TiO_2(15c) nanocomposite presents the smallest semicircle radius and the lowest charge-transfer resistance (R_{ct}). Collectively, these findings demonstrate that the ZnS/CdS/B-TiO_2(15c) nanocomposite possesses excellent photoelectrochemical performance, which can effectively facilitate the efficient separation and migration of photogenerated electrons, thereby significantly enhancing the photocathodic protection effect for 316 SS.

The band structures of ZnS, CdS, and B-TiO_2 were investigated using Mott–Schottky (M–S) analysis. As shown in Fig. 14a–c, the positive slopes observed in the M–S plots indicate that all three materials exhibit n-type semiconductor characteristics. The flat band potentials (E_{fb}) of ZnS, CdS, and B-TiO_2 were determined to be −1.02, −0.63, and −0.21 V *vs.* SCE, respectively. These values were converted to the Normal Hydrogen Electrode (NHE) scale using the equation $E_{NHE} = E_{SCE} + 0.24$ V.[53,54] Consequently, the E_{fb} values (*vs.* NHE) for ZnS, CdS, and B-TiO_2 are −0.78, −0.39, and 0.03 V, respectively. Generally, for n-type semiconductors, the conduction band potential (E_{CB}) is approximately 0.2 V more negative than the flat band potential ($E_{CB} \approx E_{fb} - 0.2$ V). Based on this, the E_{CB} levels were calculated as −0.98, −0.59, and −0.17 eV, respectively. Furthermore, combining these results with the band gap

Table 1 Comparison of the photocathodic protection performance of the as-prepared ZnS/CdS/B-TiO_2(15c) photoanode with other recently reported TiO_2-based photoanodes

Photoanode	Protected metal	Electrolyte for metal	Photo-potential (E_{CP})	Stability duration	Ref./year
ZnS/CdS/B-TiO_2(15c)	316 SS	3.5 wt% NaCl	−0.89 V	18 h	This work
Co_3O_4/TiO_2	304 SS	3.5 wt% NaCl	−0.69 V	5 h	2023 (ref. 48)
g-C_3N_4/TiO_2	Mg-Ni	3.5 wt% NaCl	−0.82 V	24 h	2025 (ref. 49)
$Bi/BiOBr/TiO_2$	316 SS	3.5 wt% NaCl	−0.43 V	3 h	2023 (ref. 50)
$MnFe_2O_4$@SiO_2/TiO_2	304 SS	0.1 M Na_2SO_4	−0.58 V	12 h	2022 (ref. 51)
$Co(OH)_2/TiO_2$	304 SS	3.5 wt% NaCl	−0.53 V	6 h	2021 (ref. 52)

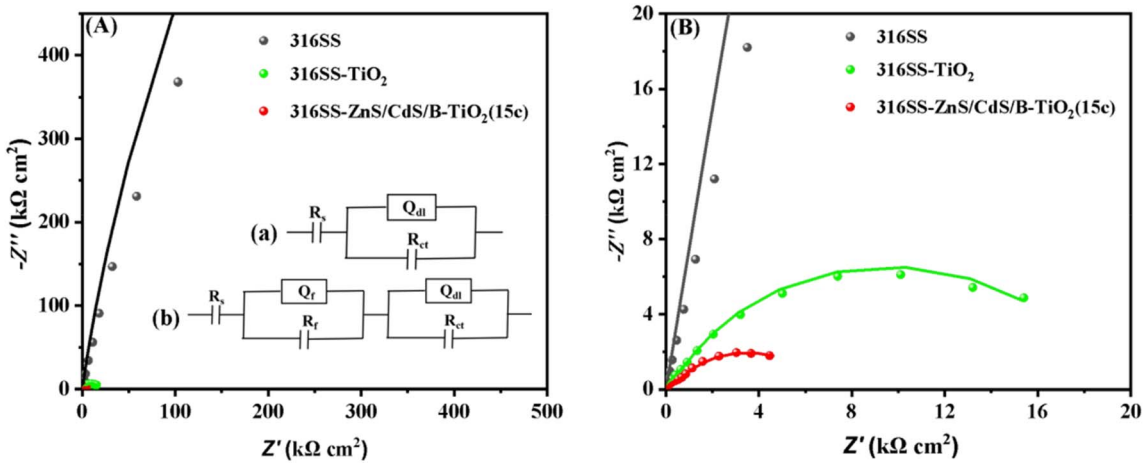

Fig. 13 (A): Nyquist plots of 316SS, 316SS-TiO_2 and 316SS-ZnS/CdS/B-TiO_2(15). (B) Magnified view of (A).

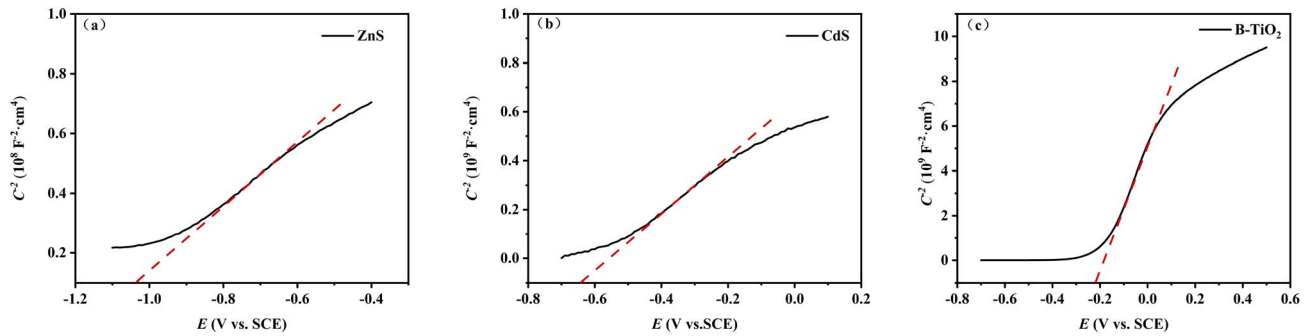

Fig. 14 Mott–Schottky curves of different photoanode materials, (a) ZnS, (b) CdS, (c) B-TiO_2.

energies (E_g)-reported as 3.68 eV for ZnS and 2.42 eV for CdS in standard literature,[55] and 2.89 eV for B-TiO_2-the valence band potentials (E_{VB}) were calculated using the equation:[56] $E_{VB} = E_{CB} + E_g$. The resulting E_{VB} positions for ZnS, CdS, and B-TiO_2 are 2.70, 1.83, and 2.72 eV, respectively.

The plausible mechanism governing the enhanced photoelectrochemical performance of the ZnS/CdS/B-TiO_2 composite photoanode is schematically illustrated in Fig. 15. Based on the band structure derived from Mott–Schottky analysis, the components form a cascade type-II heterojunction, which provides a thermodynamic driving force for efficient charge separation. Specifically, under simulated solar illumination, all three components can be excited to generate electron–hole pairs. According to the calculated band positions, the conduction band (CB) potentials of ZnS, CdS, and B-TiO_2 are located at −0.98, −0.59, and −0.17 eV (*vs.* NHE), respectively. This distinct "stepped" energy alignment facilitates a directional transfer of photogenerated electrons. Electrons excited in the CB of ZnS spontaneously migrate to the CB of CdS, and subsequently inject into the CB of B-TiO_2. Simultaneously, the electrons generated within CdS are also transferred to B-TiO_2. These accumulated electrons are then efficiently transported through the highly conductive Ti^{3+}-doped TiO_2 nanotubes to the Ti substrate and finally channeled to the 316 SS electrode *via* the

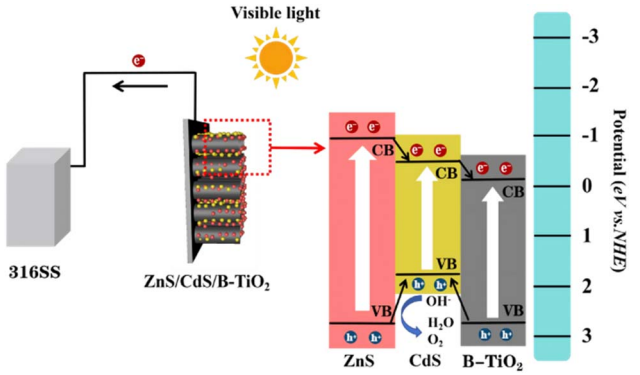

Fig. 15 Mechanism diagram of photocathodic protection.

external circuit. This continuous electron injection induces a significant negative potential shift in the coupled steel, providing effective cathodic protection. Regarding hole transport, the VB potentials of ZnS, B-TiO_2, and CdS are 2.70, 2.72, and 1.83 eV, respectively. Since holes naturally migrate towards more negative potentials, photogenerated holes in the VB of ZnS and B-TiO_2 tend to transfer to the VB of CdS. Consequently, the photogenerated holes accumulate primarily on the CdS valence band. Although this hole accumulation typically poses a risk of photocorrosion, the ZnS shell plays a critical protective role. Firstly, the ZnS overlayer effectively passivates the surface defects and dangling bonds of CdS, which are the primary active sites for self-oxidative decomposition. Secondly, ZnS acts as a physical barrier that mitigates the direct erosion of the CdS lattice by the electrolyte. Furthermore, the efficient charge separation kinetics ensures that the accumulated holes are rapidly scavenged by the sacrificial sulfide ions in the electrolyte before they can oxidize the CdS lattice. This kinetic advantage, combined with structural passivation, underpins the superior stability observed in the ZnS/CdS/B-TiO_2 photoanode. In summary, the superior performance of the ZnS/CdS/B-TiO_2 system is attributed to the synergistic effect of the cascade band alignment and Ti^{3+} self-doping. The ZnS layer, with its high CB position, acts as an upstream electron pump; CdS serves as a central visible-light absorber and charge relay station; while Ti^{3+}-doping introduces mid-gap states that improve the conductivity of TiO_2. This optimized configuration ensures rapid spatial separation of electron–hole pairs, suppresses recombination, and maximizes the utilization of photogenerated electrons for the photocathodic protection of 316 SS.

4. Conclusion

In summary, a novel ZnS/CdS/Ti^{3+} self-doped TiO_2 nanotube array photoanode was successfully constructed *via* a combination of anodic oxidation, electrochemical reduction, and SILAR techniques. The optimized ZnS/CdS/B-TiO_2(15c) composite effectively overcomes the intrinsic limitations of pristine TiO_2 by integrating Ti^{3+} self-doping defects with a cascade heterojunction. Consequently, the photoanode exhibits superior photoelectric performance, achieving a high photocurrent density of 279 μA cm^{-2} under simulated solar illumination-approximately 14 times that of pristine TiO_2. When coupled with 316 SS, it induces a significant cathodic potential drop, stabilizing the open-circuit potential at −0.89 V (*vs.* SCE), which ensures robust photocathodic protection. Mechanism analysis confirms that the enhanced performance stems from the synergistic effect of improved conductivity induced by Ti^{3+} doping and the efficient spatial separation of charge carriers driven by the stepped band alignment. This work provides a rational strategy for designing high-efficiency photoanodes for marine corrosion protection applications.

Conflicts of interest

There are no conflicts to declare.

Data availability

All data supporting the findings of this study are fully available within the article. No additional external data sources are required to replicate the research conclusions.

Acknowledgements

This study was supported by grants from the Natural Science Foundation of Shandong Province of China (ZR2016BP11, ZR2018LE002).

References

1 C. Peng, G. Cao, T. Gu, C. Wang, Z. Wang and C. Sun, The effect of dry/wet ratios on the corrosion process of the 6061 Al alloy in simulated nansha marine atmosphere, *Corros. Sci.*, 2023, **210**, 110840.
2 Y. Ma, Y. Zhang, R. Zhang, F. Guan, B. Hou and J. Duan, Microbiologically influenced corrosion of marine steels within the interaction between steel and biofilms: a brief view, *Appl. Microbiol. Biotechnol.*, 2020, **104**, 515–525.
3 Q. Xie, A. Ma, J. Jiang, H. Liu, Z. Cheng and Y. Gu, Tailoring the corrosion behavior and mechanism of AZ31 magnesium alloys by different Ca contents for marine application, *Corros. Sci.*, 2021, **192**, 109842.
4 L. Jin, X. Zhang, X. Liang, Z. Wang and Q. Wu, Mechanical properties of corroded carbon steel based on random pit corrosion in marine environment, *Ocean Eng.*, 2022, **260**, 111759.
5 J. Liu, Q. Li, F. Meng, T. Zhang, F. Gao, X. Zhan, *et al.*, Recent progress in fabrications, mechanisms and developments of photo-responsive marine antifouling coatings, *Prog. Org. Coat.*, 2024, **186**, 108070.
6 P. Jin, Z. Guan, H. Wang, X. Wang, G. Song and R. Du, Fabrication of CdSe/$ZnIn_2S_4$ modified TiO_2 nanotube composite and its application in photoelectrochemical cathodic protection, *J. Electroanal. Chem.*, 2022, **904**, 115884.
7 S. Xu, H. Zhang, Z. Zhang, Z. Li, A. Xie, P. Qiu, *et al.*, High-efficiency photocathodic protection performance of novel

TiO_2/ZnCdS heterojunction films for Q235 carbon steel, *Mater. Today Commun.*, 2024, **40**, 110125.

8 T. H. Yun, T. Kim, M. Kim, J. H. Park and S. Kim, Enhancing corrosion resistance of carbon steel and stainless steel through photocathodic protection using TiO_2-polyvinyl butyral electrophoretic deposition coating, *J. Ind. Eng. Chem.*, 2023, **126**, 408–417.

9 X. Jiang, M. Sun, Z. Chen, J. Jing and C. Feng, High-efficiency photoelectrochemical cathodic protection performance of the TiO_2/$AgInSe_2$/In_2Se_3 multijunction nanosheet array, *Corros. Sci.*, 2020, **176**, 108901.

10 D. Xu, Y. Liu, Y. Liu, F. Chen, C. Zhang and B. Liu, A review on recent progress in the development of photoelectrodes for photocathodic protection: design, properties, and prospects, *Mater. Des.*, 2021, **197**, 109235.

11 Y. Yang and Y. Cheng, Visible light illuminated high-performance WO_3-TiO_2-$BiVO_4$ nanocomposite photoanodes capable of energy self-storage for photo-induced cathodic protection, *Corros. Sci.*, 2020, **164**, 108333.

12 X. Ning, S. Ge, X. Wang, H. Li, X. Li, X. Liu, *et al.*, Preparation and photocathodic protection property of Ag_2S-TiO_2 composites, *J. Alloys Compd.*, 2017, **719**, 15–21.

13 H. Xu, W. Liu, L. Cao, G. Su and R. Duan, Preparation of porous TiO_2/ZnO composite film and its photocathodic protection properties for 304 stainless steel, *Appl. Surf. Sci.*, 2014, **301**, 508–514.

14 X. Chen, G. Zhou, X. Wang, H. Xu, C. Wang, Q. Yao, *et al.*, Progress in semiconductor materials for photocathodic protection: design strategies and applications in marine corrosion protection, *Chemosphere*, 2023, **323**, 138194.

15 Y. Dai, N. Liu, C. Wang, X. Liu, Q. Jiang, Y. Liu, *et al.*, NiCo-layered double hydroxide modified TiO_2 nanotube arrays and its application in photoelectrochemical cathodic protection of 304 stainless steel, *Colloids Surf., A*, 2024, **680**, 132633.

16 J. Cui and Y. Pei, Enhanced photocathodic protection performance of Fe_2O_3/TiO_2 heterojunction for carbon steel under simulated solar light, *J. Alloys Compd.*, 2019, **779**, 183–192.

17 Z. Ma, X. Ma, X. Wang, N. Liu, X. Liu and B. Hou, Study on the photocathodic protection of Q235 steel by $CdIn_2S_4$ sensitized TiO_2 composite in splash zone, *Electrochim. Acta*, 2019, **9**, 1067.

18 Z. Lin, Y. Lai, R. Hu, J. Li, R. Du and C. Lin, A highly efficient ZnS/CdS@TiO_2 photoelectrode for photogenerated cathodic protection of metals, *Electrochim. Acta*, 2010, **55**, 8717–8723.

19 C. Wang, R. Thompson, P. Ohodnicki, J. Baltrus and C. Matranga, Size-dependent photocatalytic reduction of CO_2 with PbS quantum dot sensitized TiO_2 heterostructured photocatalysts, *J. Mater. Chem.*, 2011, **21**, 13452–13457.

20 H. Guo, L. Li, C. Su, D. Yu and Z. Liu, Effective photocathodic protection for 304 stainless steel by PbS quantum dots modified TiO_2 nanotubes, *Mater. Chem. Phys.*, 2021, **258**, 123914.

21 D. R. Baker and P. Kamat, Photosensitization of TiO_2 nanostructures with CdS quantum dots: particulate *versus* tubular support architectures, *Adv. Funct. Mater.*, 2009, **19**, 805–811.

22 J. Zhang, R. Du, Z. Lin, Y. Zhu, Y. Guo and H. Qi, Highly efficient CdSe/CdS co-sensitized TiO_2 nanotube films for photocathodic protection of stainless steel, *Electrochim. Acta*, 2012, **83**, 59–64.

23 H. Li, X. Wang, Q. Wei and B. Hou, Photocathodic protection of 304 stainless steel by Bi_2S_3/TiO_2 nanotube films under visible light, *Nanoscale Res. Lett.*, 2017, **12**, 80.

24 Z. Guan, X. Wang, P. Jin, Y. Tang, H. Wang, G. Song, *et al.*, Enhanced photoelectrochemical performances of ZnS-Bi_2S_3/TiO_2/WO_3 composite film for photocathodic protection, *Corros. Sci.*, 2018, **143**, 31–38.

25 J. Liu, N. Wang, F. Zheng, C. Wang, J. Wang, B. Hou, *et al.*, $CuInS_2$/TiO_2 heterojunction with elevated photo-electrochemical performance for cathodic protection, *J. Mater. Sci. Technol.*, 2022, **122**, 211–218.

26 W. Wang, Z. Yang, G. Li, Y. Zhang, W. Cao, J. Xu, *et al.*, Drastic promotion of the photocathodic protection property of TiO_2 nanotube films decorated with n-type $CuInS_2$ nanoparticles, *J. Alloys Compd.*, 2022, **890**, 161895.

27 P. Priyadarshini, S. Das, S. Senapati, S. Samal, G. Pradhan and R. Naik, Preparation of nanosheets embedded ZnSe/Bi_2Se_3 core/shell quantum dots for the study of optical properties and antibacterial activity, *Surf. Interfaces*, 2023, **37**, 102687.

28 A. Parida, S. K. Samal, S. Chinnaiah and R. Naik, SnS/MnSe Heterostructures for Enhanced Optoelectronics and Dielectric Applications, *Nanoscale Adv.*, 2024, **6**, 6365–6377.

29 K. Manjunatha, D. Alagarasan, S. Das, R. Ganesan, R. Naik, D. Purohit and M. Ramudu, Influence of Substrate Temperature on $SnSe_2$/TiO_2 Heterostructure for Photodetector Applications, *Sens. Actuators, A*, 2025, **391**, 116641.

30 S. Xu, Z. Li, S. Kawi, A. Xie, P. Qiu, L. Yang, *et al.*, Fabrication of multi-layered TiO_2/CdS@ZnS nanocomposite film for highly stable and efficient photocathodic protection of carbon steel, *Mater. Today Commun.*, 2025, **42**, 111134.

31 T. Song, P. Zhang, T. Wang, A. Ali and H. Zeng, Constructing a novel strategy for controllable synthesis of corrosion resistant Ti^{3+} self-doped titanium–silicon materials with efficient hydrogen evolution activity from simulated seawater, *Nanoscale*, 2018, **10**, 2275–2284.

32 L. Fang, J. Chen, M. Zhang, X. Jiang and Z. Sun, Introduction of Ti^{3+} ions into heterostructured TiO_2 nanotree arrays for enhanced photoelectrochemical performance, *Appl. Surf. Sci.*, 2019, **490**, 1–6.

33 J. Pu, X. Wang, J. Liu, M. Ren, Y. Nan, M. Liu, *et al.*, PDA decorated spaced TiO_2 nanotube array photoanode material for photocathodic protection of 304 stainless steels, *J. Electroanal. Chem.*, 2022, **914**, 116319.

34 H. Deng, M. Huang, W. Weng and J. Lin, Photocathodic protection of iron oxide nanotube arrays fabricated on carbon steel, *Surf. Coat. Technol.*, 2015, **266**, 183–187.

35 M. Machreki, T. Chouki, G. Tyuliev, D. Zigon, B. Ohtani, A. Loukanov, *et al.*, Defective TiO_2 nanotube arrays for

efficient photoelectrochemical degradation of organic pollutants, *ACS Omega*, 2023, **8**, 21605–21617.

36 Y. Wan, M. Han, L. Yu, J. Jia and G. Yi, Fabrication and photoelectrochemical properties of TiO_2/$CuInS_2$/Bi_2S_3 core/shell/shell nanorods electrodes, *RSC Adv.*, 2015, **5**, 78902–78909.

37 X. Zheng, S. Das, Y. Gu, S. Liu and J. Zhao, Optimal engineering of CdS/PbS co-sensitized TiO_2 nanotube arrays for enhanced photoelectrochemical performance, *Ceram. Int.*, 2020, **46**, 12050–12058.

38 Z. Li, Y. Xie, H. Xu, T. Wang, Z. Xu and H. Zhang, Expanding the photoresponse range of TiO_2 nanotube arrays by CdS/CdSe/ZnS quantum dots co-modification, *J. Photochem. Photobiol., A*, 2011, **224**, 25–30.

39 J. Yu, C. Gong, Z. Wu, Y. Wu, W. Xiao, Y. Su, *et al.*, Efficient visible light-induced photoelectrocatalytic hydrogen production using CdS sensitized TiO_2 nanorods on TiO_2 nanotube arrays, *J. Mater. Chem. A*, 2015, **3**, 22218–22226.

40 Z. Zhou, M. Li, Y. Hu and Z. Chen, Enhanced electron storage capacity achieved by coupling NiO with WO_3/$BiVO_4$ for persistent photocathodic protection of 316 stainless steel, *Mater. Today Commun.*, 2024, **39**, 108768.

41 X. Yang, F. Tan, D. Wang, Q. Feng, D. Qiu, D. Dang, *et al.*, Entrapping Ru nanoparticles into TiO_2 nanotube: insight into the confinement synergy on boosting pho-thermal CO_2 methanation activity, *Ceram. Int.*, 2021, **47**, 27316–27323.

42 X. Wang, M. Lian, X. Yang, P. Lu, J. Zhou and L. Miao, Enhanced activity for catalytic combustion of ethylene by the Pt nanoparticles confined in TiO_2 nanotube with surface oxygen vacancy, *Ceram. Int.*, 2022, **48**, 3933–3940.

43 P. Priyadarshini, D. Sahoo, D. Alagarasan, S. Varadharajaperumal, R. Ganesan and R. Naik, Structural and optoelectronic properties change in Bi/In_2Se_3 heterostructure films by thermal annealing and laser irradiation, *J. Appl. Phys.*, 2021, **129**, 223101.

44 R. Naik and R. Ganesan, Effect of compositional variations on the optical properties of $Sb_xSe_{60-x}S_{40}$ thin films, *Thin Solid Films*, 2015, **579**, 95–102.

45 Y. Lei, L. Zhang, G. Meng, G. Li, X. Zhang, C. Liang, *et al.*, Preparation and Photoluminescence of Highly Ordered TiO_2 Nanowire Arrays, *Appl. Phys. Lett.*, 2001, **78**(8), 1125–1127.

46 M. Sun, Z. Chen and Y. Bu, Enhanced photoelectrochemical cathodic protection performance of the C_3N_4@In_2O_3 nanocomposite with quasi-shell–core structure under visible light, *J. Alloys Compd.*, 2015, **618**, 734–741.

47 L. Zhang, X. Wang, H. Li, H. Sun, N. Zhuang and B. Hou, Photogenerated cathodic protection properties of CdSe-TiO_2 composite material on 304 stainless steel, *Corros. Prot.*, 2015, **36**, 258–262.

48 X. Li, X. Wang, Y. Nan, Y. Sun, H. Xu and L. Chi, Effect of Co_3O_4/TiO_2 heterojunction photoanode with enhanced photocathodic protection on 304 stainless steel under visible light, *Colloids Surf., A*, 2023, **664**, 131150.

49 Z. Xie, Y. Wen, H. Yao, Y. Liu, G. Yu and C. Zhang, A Z-scheme g-C_3N_4/TiO_2 heterojunction for enhanced performance in protecting magnesium and nickel couple from galvanic corrosion, *Appl. Surf. Sci.*, 2025, **1010**, 177463.

50 W. Cao, W. Wang, Z. Yang, W. Wang, W. Chen and K. Wu, Enhancing photocathodic protection performance by controlled synthesis of Bi/BiOBr/TiO_2 NTAs Z-scheme heterojunction films, *Appl. Surf. Sci.*, 2023, **960**, 170675.

51 Y. Sun, X. Wang, F. Du, J. Niu, Y. Nan, J. Pu, Y. Huang and B. Hou, Fabrication of Z-scheme $MnFe_2O_4$@SiO_2/TiO_2 composite used for 304 stainless steel photocathodic protection, *J. Electroanal. Chem.*, 2022, **923**, 116813.

52 X. Lu, L. Liu, J. Ge, Y. Cui and F. Wang, Morphology controlled synthesis of $Co(OH)_2$/TiO_2 p–n heterojunction photoelectrodes for efficient photocathodic protection of 304 stainless steel, *Appl. Surf. Sci.*, 2021, **537**, 148002.

53 Z. Duan, X. Zhao, C. Wei and L. Miao, Ag-Bi/$BiVO_4$ chain-like hollow microstructures with enhanced photocatalytic activity for CO_2 conversion, *Appl. Catal., A*, 2020, **594**, 117459.

54 C. Wang, W. Gao, N. Liu, Y. Xin, X. Liu and X. Wang, Covalent organic framework decorated TiO_2 nanotube arrays for photoelectrochemical cathodic protection of steel, *Corros. Sci.*, 2020, **176**, 108920.

55 S. M. Sze and K. K. Ng, *Physics of Semiconductor Devices*, Wiley-Interscience, Hoboken, NJ, 3rd edn, 2006.

56 B. Rong, Y. Wei, X. Chen, Y. Ding, Y. Chen and H. Liu, Electron transport improvement of perovskite solar cells *via* intercalation of Na doped TiO_2 from metal-organic framework MIL-125 (Ti), *Appl. Surf. Sci.*, 2022, **574**, 151735.